communications earth & environment

Article

https://doi.org/10.1038/s43247-024-01507-3

Retrospective performance analysis of a ground shaking early warning system for the 2023 Turkey–Syria earthquake

Check for updates

Raffaele Rea [1], Simona Colombelli [1], Luca Elia [1,2] & Aldo Zollo [1]

Recently developed earthquake early warning systems rely on the idea of combining the measured ground motion and the source parameter estimate to issue an alert based on the ground shaking prediction at sites where high potential damage is expected. Here we apply a P-wave, shaking-forecast method that can track and alert in real-time the area where peak ground motion is expected to exceed a user-set threshold during the earthquake. The system performance in providing a fast and reliable warning during the Mw 7.8, February 6 Turkey–Syria earthquake is investigated by the real-time simulated playback of the near-source hundred accelerograms. With an instrumental intensity threshold $I_{MM} = IV$ an alert issued 10–20 s after the event origin, results in 95% of successful warning (positive and negative) and lead-times of 10–60 s within the potential damage zone. Setting a higher intensity threshold requires larger alert times (50–60 s) to achieve 90% of successful warning and overall shorter lead-times. Our simulation shows that the P-wave predicted, strong-shaking zone can be rapidly detected only 20 s after the mainshock nucleation. As the time increases, it well delineates the NE-SW bi-lateral rupture development as inferred by kinematic source models.

An Earthquake Early Warning System (EEWS) is an advanced monitoring infrastructure designed to detect earthquakes and provide warning of the potential damage, allowing people and automated systems to take precautionary measures before the arrival of destructive seismic waves. The primary goal of an EEWS is to mitigate the potential impact of earthquakes by providing timely and accurate information to individuals, organizations, and infrastructures allowing to take protective actions such as seeking cover, shutting down critical systems, initiating emergency protocols, or evacuating vulnerable areas. It also offers an opportunity for automated systems to activate safety measures, such as stopping trains, closing gas valves, or halting industrial operations, minimizing the risk of injury, damage, and loss of life.

Countries located in seismically active regions are at the forefront of implementing EEWS. Japan's system, known as the Japan Meteorological Agency's Earthquake Early Warning, has been operational since 2007 and has played a crucial role in mitigating the impact of earthquakes[1]. Other countries, including Mexico, the United States, Taiwan, and China, have also developed and deployed their own systems, each tailored to their specific seismic activity patterns and infrastructure needs[2].

During the last two decades in Europe, EEWS have been developed and tested in active seismic countries, along the Mediterranean region (Italy, Romania, Switzerland, Turkey, Greece, and the Ibero-Maghrebian region), mainly for research purposes, while the technological components of the operational seismic monitoring systems are yet not fully real-time compliant, such that they can be an effective tool for fast seismic risk mitigation actions[3].

Network-based EEWS have been recently classified as source- or wavefield-based regional systems[4].

Source-based EEWS make use of a network of seismic sensors densely placed in earthquake-prone regions to detect initial earthquake waves, analyze the data, and estimate the magnitude and location of the event. The earthquake shaking potential is predicted through specific, regional Ground Motion Prediction Equations, GMPE to nearby and distant sites, using previously calibrated empirical attenuation relationships. Alternatively, the *wavefield-based* EEWS aim at computing and tracking the space-time evolution of the peak ground motion over an expanding epicentral area using physics-based, spatial interpolating algorithms that used continuously updated measures at a dense acceleration network. In this case, the alert is issued to sites where a peak ground motion threshold is exceeded, without needing for source parameter determination.

With the idea to integrate source- and wavefield-based approaches, recently ref. 5 proposed a new P-wave, shaking-forecast-based EEW method based on the real-time, evolutionary mapping of the Potential Damage (or strong shaking) Zone (PDZ) as represented by the epicentral area where a

[1]Department of Physics E. Pancini, University of Naples Federico II, Naples, Italy. [2]Istituto Nazionale di Geofisica e Vulcanologia, Sezione di Napoli Osservatorio Vesuviano, Naples, Italy. e-mail: aldo.zollo@unina.it

predicted Intensity Measure (IM), such as the peak ground velocity/acceleration or the instrumental intensity, exceeds a pre-set threshold during the earthquake occurrence. The methodology includes refined estimations of the main source parameters (earthquake location and magnitude) and P-wave-based, peak motion predictions[6–8] that are used to assess the expected shaking level at not instrumented sites. In this paper, we illustrate the results of a retrospective analysis of the performance of this shaking-forecast-based EEW method in terms of successful and failed alerts, by simulating the real-time recordings of the recent destructive 2023, February 6, Mw 7.8 earthquake, occurred at the frontier between Turkey and Syria, that caused by the multiple rupture of several segments of the Eastern Anatolian fault (EAF).

EAF is one of the major fault systems in Turkey, extending for approximately 600 km across the eastern part of the country. It is a left-lateral strike-slip fault that accommodates the tectonic movement between the Arabian and Anatolian microplates with a strain rate of about 10 mm/yr[9]. The EAF forms part of the larger complex tectonic boundary system in the region, including the North Anatolian Fault (NAF) to the west and the Dead Sea Transform Fault to the southeast. On February 6, 2023, at 4:17 a.m. the first earthquake of magnitude 7.8 struck the city of Pazarcık in south-central Turkey and, about 9 h later (at 1:24 p.m.), a second shock of magnitude 7.6 occurred with an epicenter near the city of Elbistan, about 100 km north of the mainshock epicenter. The first earthquake rupture had an extent of about 350 km while the second event ruptured a secondary branch of the EAF, EW trending fault about 250 km long[10]. At depth, the aftershocks mainly distribute in the shallow crustal layer between 3 and 7 km depth. During the two rupture episodes the average dislocation was estimated to vary between 2 and 6 meters[10,11]. A large area was affected by shaking whose instrumental intensity was higher than $I_{MM} = VII$, with peaks of $I_{MM} = IX$ and X (US Geological Survey[12]). Indeed, damage was found in an area of about 350,000 km^2 with 14 million people, or 16% of Turkey's population, being affected (according to Disaster and Emergency Management Authority, https://en.afad.gov.tr/press-bulletin-27-about-the-earthquake-in-kahramanmaras). This event represented the deadliest earthquake in Turkey's history since the Antioch earthquake of 526 and in present-day Syria since the Aleppo earthquake of 1822 with a confirmed death toll of about 59,000 of which 51,000 in Turkey and 8000 in Syria, according to Disaster and Emergency Management Presidency (AFAD). The dense Turkey accelerometer network (owned and operated by AFAD) recorded high peak acceleration values (larger than 0.2–0.3 g) in a large area around the epicenters of the earthquake showing a southwest/northeast elongation of the high peak acceleration area (US Geological Survey, event page of the 7.8 Kahramanmaraş Earthquake Sequence). Acceleration signals recorded by stations located along the EAF fault showed clear evidence for a complex, bi-lateral rupture propagation during the two mainshocks.

Here we performed the offline retrospective analysis of the early warning method during the Mw 7.8 event, by using the accelerometric data provided by the AFAD agency. We used the 3-component records from 110 stations in the area (Fig. 1) between 20 and 300 km from the epicenter and simulated the real-time streaming of data into the system to assess the potential performance of an early warning system for such a disastrous event. The epicentral area of about 300 km radius, experienced PGV > 5 cm/s and along-fault regions with PGV > 50 cm/s that corresponds to a perceived shaking between moderate to severe in the USGS shakemap instrumental intensity scale.

Results

The methodology combines several modules, from earthquake detection/location to magnitude determination and peak ground shaking prediction[5]. The adopted strategy combines the principles of onsite EEW methods (Peak ground shaking prediction by P-wave amplitude measurements) with those of a network-based approach (real-time location, magnitude estimation and PGV prediction through regional-specific GMPEs) (see Methods). Figure 2 shows the time evolution of the earthquake location (2a) and moment magnitude (2b) estimates. Both parameters are determined from each strong motion record using the automatically detected P wave arrival time and peak amplitude every 0.5 s, as the P-wavefront propagates across the array of stations. The estimate of magnitude requires a previous earthquake location (eq. 1S in Supplementary Information) and are available at different times, at stations located at increasing epicentral distances.

Both earthquake location and magnitude converge to stable estimates after 50–60 s from the origin time.

As for the location, it stabilizes at about 20 s (Fig. 1a) after the OT, with an accurate epicenter determination (error = 3 km) but an uncertain depth value (error = 10 km). The error is defined as the difference in epicentral distance and depth between the real-time determined solution and the USGS bulletin values of parameters.

As for the magnitude (Fig. 1b), all station curves (gray lines) show a common, characteristic behavior versus time, with an initial, near-monotonic increase till reaching a plateau level, which corresponds to the maximum estimated magnitude. This trend is consistent with worldwide observations for different magnitude earthquakes of the time-evolving, P-wave magnitude as determined from the log-displacement amplitude measured in an expanded time window, which is associated with time-evolutive apparent source time function up to its peak value is achieved[13–15]. Despite a similar trend, the station magnitude curves show a variability which is caused by azimuthal/distance source and propagation effects that are not properly accounted by the isotropic linear empirical relation between the observed displacement amplitude and magnitude/distance.

The blue curve in Fig. 2 quantifies the average magnitude estimated at each time step. After an initial underestimation (M about 6.6) the magnitude converges in 40–50 s to a stable value ($\boldsymbol{M_W}$ 7.5). The final estimated magnitude underestimates the teleseismic moment-tensor derived $\boldsymbol{M_W}$ estimation ($\boldsymbol{M_W}$ 7.8), but well compares to body-wave teleseismic mB and Mwp (7.2–7.4) as inferred by different seismological agencies[16].

Since the rupture initiated on the secondary Narli fault and then propagated toward the EAf[10,11] the initial magnitude (M6.6) may reflect the earthquake magnitude associated with the initial rupture of the Narli fault segment. The slow convergence to a stable value for the magnitude estimation is likely due to low energy release during the initial phase of the rupture process, as it confirmed by the moment rate functions determined by different authors[10,17], showing a slow growth of the moment rate function, and reaching the peak value (corresponding to a $\boldsymbol{M_W}$ 7.8) only 60 s after the origin time.

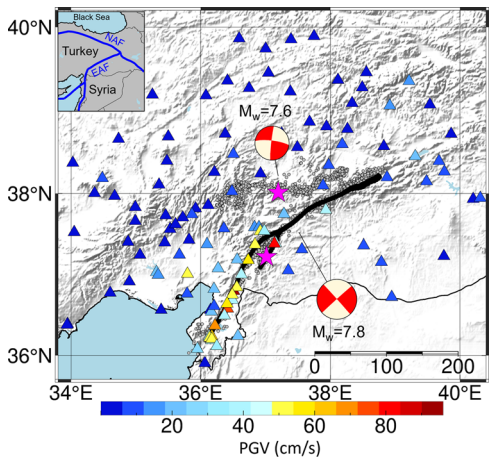

Fig. 1 | Map of the studied area with M7.8 and M7.6 mainshock/aftershock and strong motion station locations. The figure reports the epicenter location of the two main events (magenta stars) along with their focal mechanism[12], the fault associated with the magnitude 7.8 event (solid, black line) and the aftershock locations[10] (gray dots). The triangles indicate the location of the strong-motion stations used in this study with a color representing the peak ground velocity (PGV) recorded from the magnitude 7.8 earthquake. The inset map illustrates the large-scale main geographical and seismotectonic elements of the area under study (the blue lines indicate the East Anatolian Fault and the North Anatolian Fault).

The performance of the EEW method is evaluated in terms of its quickness in issuing the alert, the amount of available lead-time (e.g., the time available for emergency safety action before the occurrence of strong shaking) and the goodness of the impact prediction. As the P-wave propagates within the seismic network, its amplitude is continuously measured along the P-wave time window and used to estimate the event magnitude and to predict the PGV at the instrumented site through region-specific PGV vs P_a, P_v, P_d empirical relations (see Methods and Supplementary Information). For a given threshold of PGV, the Time of the First Alert (TFA) is defined as the time at which the predicted PGV exceeds the threshold. Here we used two thresholds calibrated according to the relative instrumental Intensity ($\boldsymbol{I_{MM}}$): PGV = 0.21 cm/s (for $\boldsymbol{I_{MM}}$=***IV***) and PGV = 1.46 cm/s (for $\boldsymbol{I_{MM}}$=***VI***)[18]. Results obtained using different PGV-to-I_{MM} scaling relationships are shown in the Supplementary Information (Text S2 and Figs. S3–S8).

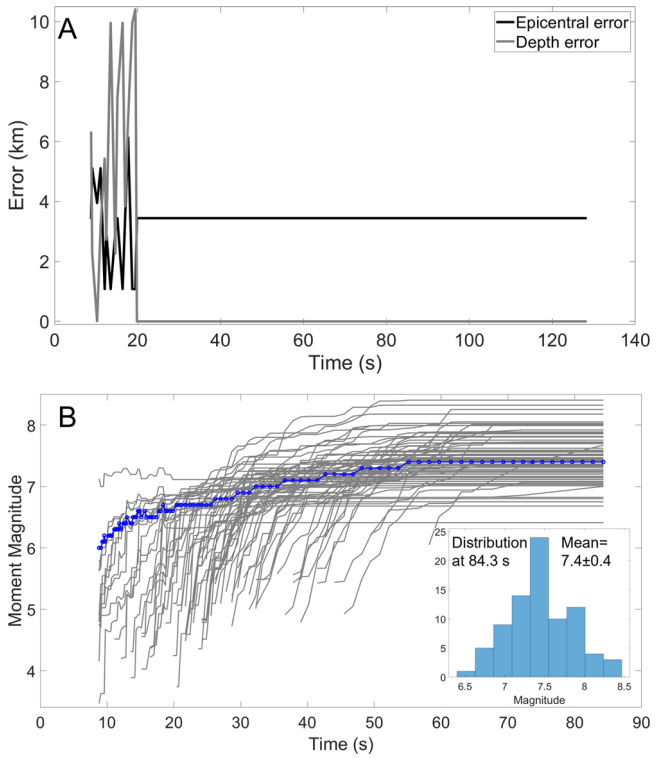

Fig. 2 | Time evolution of the moment magnitude and location parameter estimations. A Epicentral (gray curve) and depth (black curve) error as a function of the time. The error is defined as the distance in km between the estimated epicenter coordinates/depth and the corresponding USGS bulletin values. **B** The magnitude evolution with time at each recording station (gray curves) as measured from the P-wave peak amplitude in an expanded window starting at the first P-arrival and ending at the theoretical estimated S arrival. The average magnitude along with uncertainty is plotted with a blue color. In this panel we also show the distribution of the estimations of the magnitude at the end of the simulation.

The goodness of impact prediction by our EEW method is assessed by comparing the observed and predicted I_{MM} intensity (estimated from PGV) as exceeding or not exceeding a user-defined threshold. We adopted the following definitions:

$$\text{Successful Alert(SA)} : \mathbf{I}_{\mathbf{MM}}^{\mathbf{pred}} \geq \mathbf{I}_{\mathbf{MM}}^{\mathbf{thre}} \,\&\, \mathbf{I}_{\mathbf{MM}}^{\mathbf{obs}} \geq \mathbf{I}_{\mathbf{MM}}^{\mathbf{thre}};$$

$$\textit{Successful No} - \textit{Alert(SNA)} : \mathbf{I}_{\mathbf{MM}}^{\mathbf{pred}} < \mathbf{I}_{\mathbf{MM}}^{\mathbf{thre}} \,\&\, \mathbf{I}_{\mathbf{MM}}^{\mathbf{obs}} < \mathbf{I}_{\mathbf{MM}}^{\mathbf{thre}};$$

$$\textit{Missed Alert(MA)} : \mathbf{I}_{\mathbf{MM}}^{\mathbf{pred}} < \mathbf{I}_{\mathbf{MM}}^{\mathbf{thre}} \,\&\, \mathbf{I}_{\mathbf{MM}}^{\mathbf{obs}} \geq \mathbf{I}_{\mathbf{MM}}^{\mathbf{thre}};$$

$$\text{False Alert(FA)} : \mathbf{I}_{\mathbf{MM}}^{\mathbf{pred}} \geq \mathbf{I}_{\mathbf{MM}}^{\mathbf{thre}} \,\&\, \mathbf{I}_{\mathbf{MM}}^{\mathbf{obs}} < \mathbf{I}_{\mathbf{MM}}^{\mathbf{thre}}$$

$$(\text{where } \boldsymbol{I_{MM}^{thre}} = \boldsymbol{IV} \textbf{ or } \boldsymbol{VI})$$

Using this decision matrix, we can evaluate the percentage of Successful Alerts (SA), Successful No-Alerts (SNA), False Alerts (FA) and Missed Alerts (MA), by comparing the predicted and observed intensities at the 110 network stations as a function of the time after the OT (Fig. 3a, b). In both panels of Fig. 3, the first estimated quantities are obtained at the time T_{Fisrt} = 8.8 s, that corresponds to the time of the first location/magnitude estimation obtained from the automatic analysis of the early P-wave signals at the 10 stations nearest to the epicenter.

As expected, the system performance in terms of SA + SNA, FA and MA evolves with time. If we consider the lower intensity threshold ($\boldsymbol{I_{MM}}$=***IV***), at all times after T_{First} the percentage of successful alerts and no-alerts (SA + SNA) is always greater than 85% and reaches a stable 100% performance at about 60 s after OT (50 s after T_{First}). All sites experience successful (dark green) or missed (red) alerts, with no successful no-alert (light green) and false (yellow) alerts. The lack of successful no-alert and false alerts is likely due to the chosen intensity thresholds, which are both small, relative to the observed shaking level and spatial distribution.

For the larger intensity threshold ($\boldsymbol{I_{MM}}$=***IV***), during the first 35 s, the initial percentage of MA largely dominates over SA + SNA, but it rapidly decreases in favor of an increased percentage of SA + SNA. At about 60 s, the number of SA + SNA stabilizes at about 90% with the remaining stations mostly characterized by FA, with zero MA.

Figure 4 shows the time of predicted (green circle) and observed (red circles) PGV exceeding the threshold at all stations as a function of the epicentral distance, for both the considered intensity thresholds. The vertical segments joining the two circles quantify the lead-times.

Results show a general increase of the lead-time with epicentral distance with the largest values observed for the smaller intensity threshold. Even considering the larger intensity threshold, the system can provide lead-times of 20–40 s at epicentral distances between 100 and 300 km where sites experimented a moderate-to-strong shaking.

Figure 5 shows the impact prediction maps at different times after OT (15 s, 30 s and 70 s) and for the two chosen intensity thresholds (I_{MM} = IV, left panels; I_{MM} = VI, right panels). We observe that adopting the lower intensity threshold, at 15 and 30 s after OT, most sites experience a

Fig. 3 | Time evolution of the alert performance. **A–B** Percentage of Successful Alerts (SA), Successful No Alerts (SNA), False Alerts (FA) and Missed Alerts (MA) versus time for two intensity thresholds ($I_{MM} = IV$ and $I_{MM} = VI$).

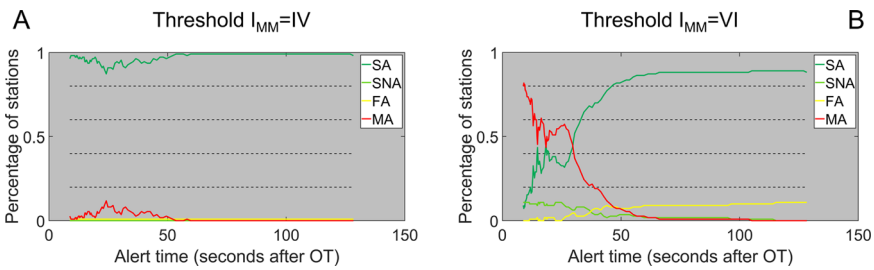

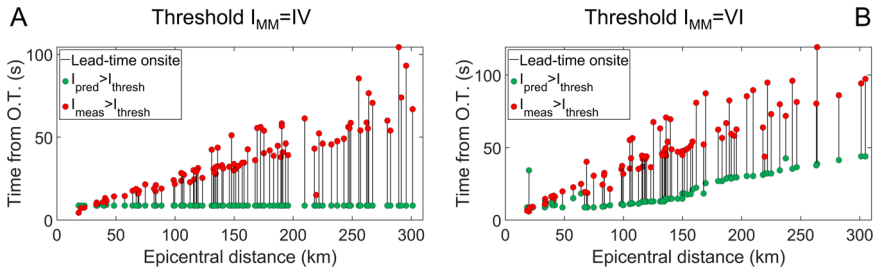

Fig. 4 | Lead times versus epicentral distance. **A** The figure shows the time (measured since the event origin time, O.T.) at which the predicted PGV exceeds the threshold $I_{MM} = IV$ (green circles) and the time at which the measured PGV exceeded the same threshold (red circles), at each station for the investigated distance range. The segments connecting the points represent the lead-time potentially available at each distance to take risk mitigation actions. **B** Same as in figure **A** but using a larger instrumental intensity threshold $I_{MM} = VI$.

successful (dark green) predicted intensity while a few remaining sites are characterized by missed alerts (red) where an underestimated peak ground shaking amplitude is predicted. Comparing the MA station location and the approximate position of the P-wavefront (yellow circle in Fig. 5), we infer that the shaking level underestimation is likely due to the combined effect of magnitude underestimation and insufficient length of recorded P-wave signal at MA sites. 70 s after OT the shaking predictions are successful at all sites of the strong motion network, since at all sites a sufficiently long P-window is recorded to obtain reliable shaking predictions above the thresholds. The lack of SNA and FA is due to the to the high observed shaking level relative to the low intensity thresholds.

Choosing a higher intensity threshold, at times 15 s and 30 s after OT, the number of MAs is higher or comparable to SA+SNAs while a relatively small number of SNAs and FA is observed (see Fig. 3A, B).

At these times, GMPE-predicted PGVs underestimate the observed shaking in sites not yet reached by the P-wavefront, because of the initial magnitude underestimation. On the other hand, at sites reached by the P-wavefront, the available window of P-signal is too short for achieving the sufficient shaking level, given the higher intensity threshold. We note that with the time increasing, sites that at 15 s were declared SNA, at 15 s changes to FA. This is due to the further shaking prediction revision, using an updated larger magnitude estimation and onsite shaking prediction using a larger P-wave time window. Later (70 s after OT), most sites evolve in SA, while the remaining 10% of sites are FA as derived from a previous SNA declaration.

Discussion

In the applied shaking-forecast based EEW method, an alert is declared at any site located within 300 km epicentral distance, where the time-evolutive, predicted $\boldsymbol{I_{MM}}$ exceeds a previous defined amplitude, at not-instrumented sites both GMPE- and onsite- PGV predictions at closest stations are combined to predict the $\boldsymbol{I_{MM}}$.

The retrospective method application to the February, 6, 2023 Mw 7.8 Turkey–Syria earthquake shows the feasibility of a P-wave, network-based system of alert which grounds on the strong motion records acquired by a dense array covering most of the high-risk areas of the country. This is the typical acquisition lay-out of strong motion networks in most of high seismic hazard zones worldwide, including Japan, China, USA and many countries in Europe of strong-motion based EWS in each of the mentioned countries.

For the analyzed case, the system performance has been evaluated considering both the quickness of the issued alarm and the goodness/robustness of the impact prediction in terms of successful, missed and false alerts. These two conditions must be considered together to assess the performance of an early warning system. The advantage of a retrospective analysis by running in playback the records of moderate to large earthquakes impacting a given seismic zone, is that the recorded peak ground motion can provide a quantitative assessment of the system robustness and reliability in term of successful and missed/false alert.

The application to the Mw7.8 Turkey–Syria mainshock records shows that our P-wave based shaking forecast EWS, depending on the chosen intensity threshold ($\boldsymbol{I_{MM}}$=$\boldsymbol{IV}$ or $\boldsymbol{I_{MM}}$=$\boldsymbol{VI}$), would have provided lead-times between 2 s, and 80 s at epicentral distances 30–50 km and 300 km, respectively. For sites at distances larger than 75 km, these lead-times reduces if the alert is required to be confirmed by the local recording of the P-wave amplitude. In this case the lead-times vary between 2 s and 40 s for epicentral distances of 30–50 km and 300 km, respectively.

The choice of the operational threshold (PGV or $\boldsymbol{I_{MM}}$) determines the rapidity with which the alert is issued but also the quality of the EEWS strong shaking prediction. A threshold of $\boldsymbol{I_{MM}}$=$\boldsymbol{IV}$ (corresponding to PGV = 0.21 cm/s from Faenza & Michelini[17]) maximizes the ratio between successful and missed/false alerts. On the contrary, setting a higher $\boldsymbol{I_{MM}}$ threshold, a large number (50% or more depending on the time of alert) of initial missed alerts are expected, especially at large distances form the source.

This is mainly caused by the initial underestimation of the GMPE- and onsite-predicted PGV, due to the insufficient extent (10 s for the first 12 stations to declare the alert) of the analyzed P-wave window as relative to the source time duration of the earthquake (60 s, Melgar et al.[10]). However, as time increases, the EW system improves the quality of predictions, since a larger P-wave time window is processed at near and far source stations, as the P-wavefront propagates across the strong motion array.

This behavior is characteristic of network-based, time-evolutive early warning systems where the impact prediction improves with the recording of wider windows of P-signal at an increasing number of more and more distant stations. A user who decides to operate the EEW system setting a low intensity threshold must comply with a frequent, relatively high number of false warnings, in particular at large distances of a moderate size event ($\boldsymbol{M_W}$ 5–6). But in cases of large earthquakes ($\boldsymbol{M_W}$ 7 +) the system achieves an extremely high percentage of successful alerts, as for the Mw 7.8 Turkey–Syria mainshock analyzed in this study. On the other hand, the conservative choice of a high intensity threshold leads to a large percentage of successful (positive/negative) alerts in case of moderate size events, while an initial large number of missed alerts is expected for large events, especially at sites distant from the source. In this case, the number of missed alerts will tend to decrease with time as longer P-signal windows are processed and new farther station records are reached by the P wavefront. In the two cases (i.e., for the low and high intensity thresholds), the decision-making strategy based on the warning could consider two possibilities: issuing the alerts to all the stations in the network (basing on the first stations that detected the event) or waiting for the P-wave to reach the station to predict more accurately the PGV, although reducing the time to take mitigation actions.

One main advantage of the proposed EEW method is that, in case of a dense strong motion array deployed in the wide earthquake source region, the PGV predicted by the near-fault, recorded P-wave amplitudes may be sensitive and allow the tracking of the rupture propagation, thus naturally accounting for source complexity[5]. The rupture kinematics of the Mw 7.8 Turkey–Syria earthquake has been extensively studied based on multi-parametric datasets (short-period, broadband seismic data, GNSS, InSAR geodetic data) and using different inversion and modeling approaches[10,19–22].

Overall, all the retrieved rupture kinematic models show that the Mw 7.8 mainshock fracture initiated along a minor branch of the East Anatolian Fault (EAF) (along the Nurdagi-Pazarcik Fault) and propagated, during the first 25 s, mainly north-eastwards along the EAF. At later times the rupture started to propagate bi-laterally both in NE and SW directions. All studies agree in showing that the largest amount of slip was released in the NE part of the fractured fault, but significant slip and its associated high seismic frequencies radiation occurred along the late activated, southern segment of the EAF[10].

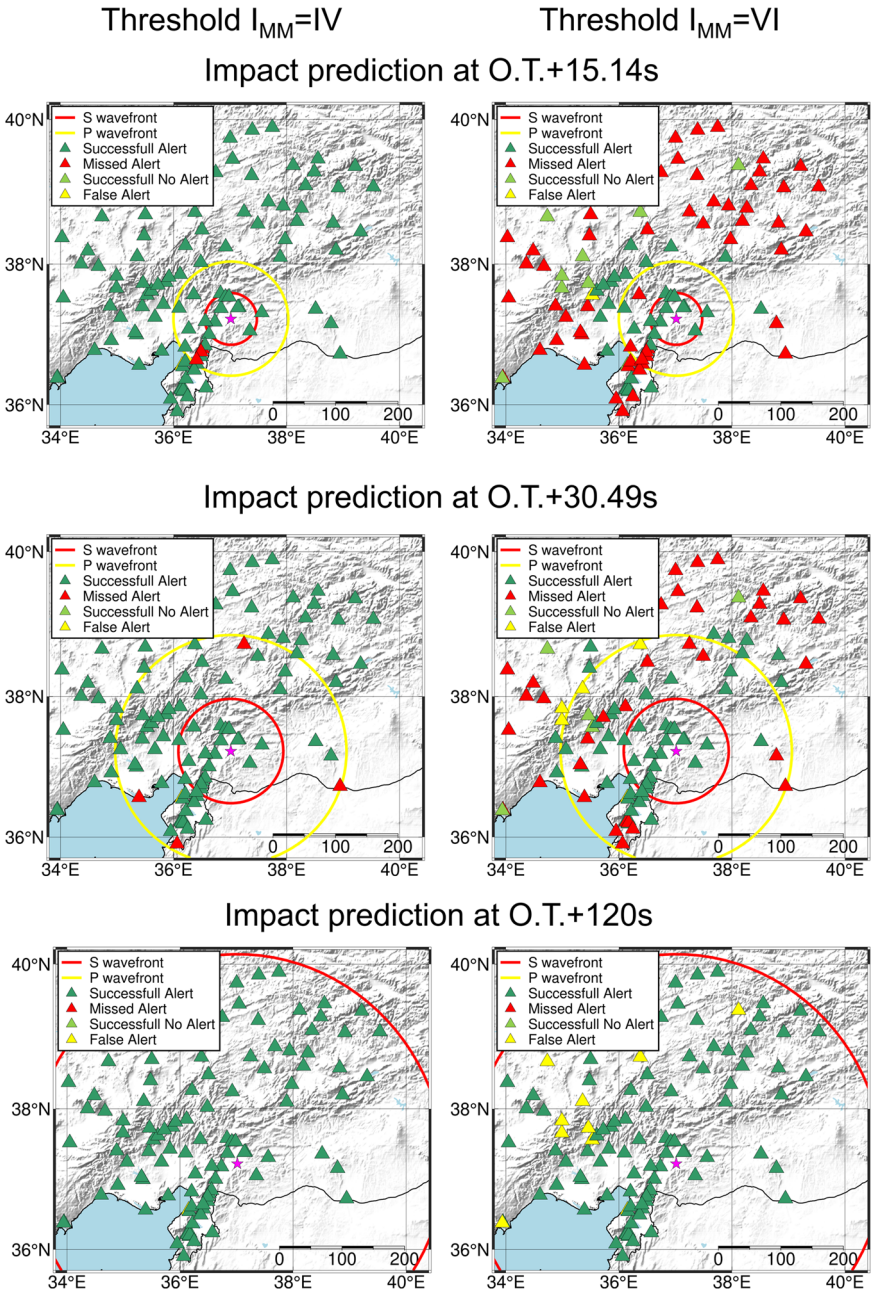

Fig. 5 | Maps of impact predictions at different times. The maps of the impact prediction are presented in terms of successful, misses and false alerts at three different times after OT and for the two considered I_{MM} = IV and I_{MM} = VI thresholds for the alert. Every station in the area is represented as a triangle with a different color based on the alert, while the epicenter is indicated with a magenta star. The red circle represents the S-wavefront, and the yellow circle represents the P-wavefront.

Figure 6 shows the snapshots of the P-wave based, instrumental intensity shake-map at different times after the OT. Our simulations show that the predicted strong-shaking zone associated to IMM intensities larger than VIII (red contour line) has been detected and tracked in the epicentral area about 20 s after the mainshock origin time, and then progressively expanded toward NE and SW, along directions that are well correlated with the main rupture propagation path. Comparing the ref. 10 kinematic rupture model of the Mw 7.8 Turkey–Syria mainshock and the time-evolving P-wave IMM VIII+ strong-shaking zone, we observe a close relation between the rupture development and the P-wave based shake map evolution with time.

At 8–10 s the strong-shaking zone is well located in the epicentral area of the mainshock, on the lateral secondary Nurdagi-Pazarcik fault of the EAF. 20 s later (30 s after OT) a strong-shaking patch appears located 31 km NE of the epicenter well located along the northern segment of the ruptured EAF. 15 s later (41 s after OT) a strong-shaking zone appears 21 km SW of the epicenter coherent with the starting of rupture propagation along the southern segment of the EAF. This pattern is confirmed 46 s later (91 s after OT) with a strong-shaking zone more elongated toward the southern portion of the EAF. During these two-time frames, we do not observe a development of the strong-shaking zone further to the North along the EAF although a general predicted IMM increase is observed at North-Eastern stations closest for the fault trace.

The close relation between the P-wave based, predicted strong shaking and the kinematic rupture development confirms the P-wave motion sensitivity to capture the source rupture complex evolution[23] with the advantage of obtaining the information on the ongoing rupture kinematics before the strong ground shaking carried out by late S and surface waves. This observation opens future perspectives for new early warning and rapid response system developments, where the P-wavefield of moderate to large earthquakes that is continuously recorded by a dense seismic array can be processed and assimilated in real-time to infer evolutionary kinematic models of the ongoing rupture process and use them for predicting the future strong shaking in the potential damaging area with a better accuracy of currently adopted empirical ground motion equations.

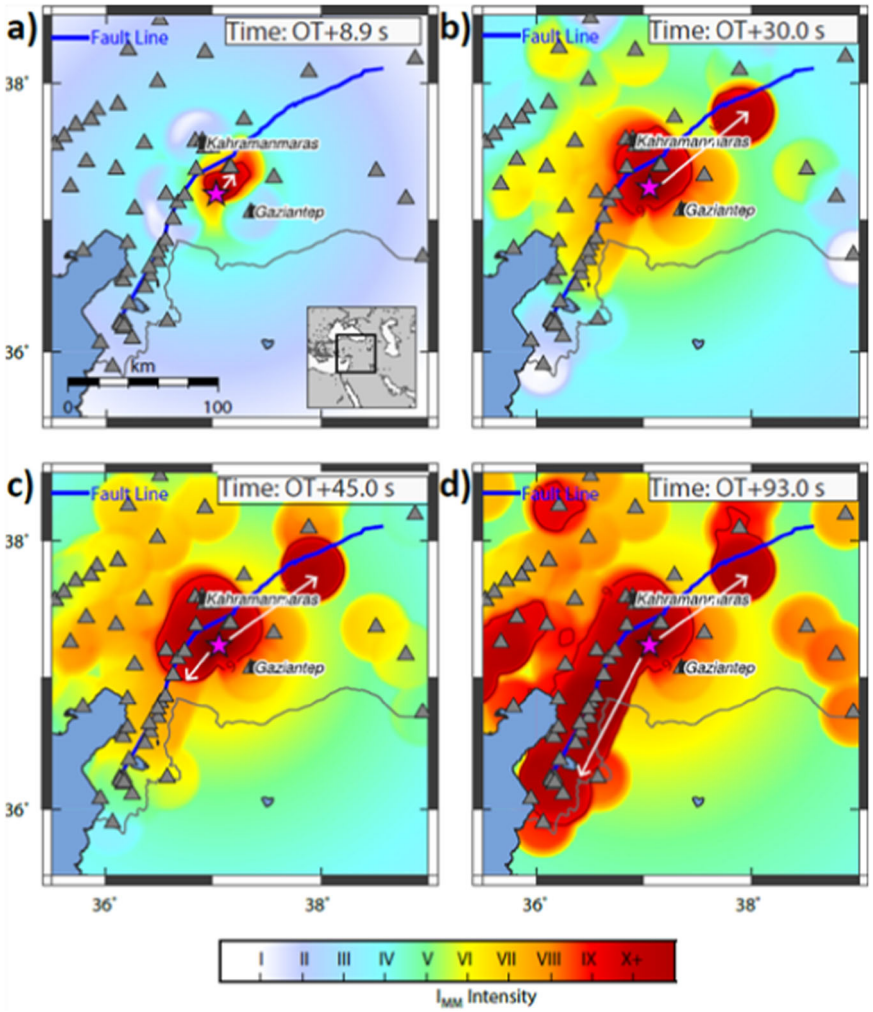

Fig. 6 | P-wave-based ground shaking maps versus time from the event origin. a Snapshot of the P-wave based shake-map of the Mw 7.8, February 6, 2023 Turkey–Syria earthquake computed at 8.9 s after the event origin time (OT). At this time the system detects the event occurrence and, using the near-epicenter P-signal records, starts the calculation of the location, magnitude and predicted $PGV - I_{MM}$. **b** 30 s after the origin time, the intensity IX+ (dark red color) zone extends in the northern direction along the EAF, pointing out the initial rupture direction. **c** 45 s after the origin time, the IX+ zone begins to expand bi-laterally along the southern segment of the EAF. **d** At the end of the event (about 90 s after OT) the intensity IX+ zone well delineates the entire rupture zone along the EAF. The evolution of the maximum intensity zone showed in this figure and in the Supplementary Video 1 agrees with the kinematic source models (e.g., Melgar et al.[10], Palo and Zollo[22]).

Conclusions

Using the waveform data recorded by the AFAD strong motion network in Turkey, we investigated the performance of an early warning method based on the time-evolutive tracking of the potential damage zone, defined as the area where a user-set peak ground motion threshold is expected to be exceeded during the earthquake. At each time step after the first recorded P-wave arrival, the method combines onsite- and GMPE-predictions to estimate the peak ground velocity at any node of a grid mapping the epicentral area. Continuously updated estimations of the earthquake location and magnitude are used to refine the GMPE-predicted PGVs, while onsite estimates are updated by expanding the P-wave time window at each recording site.

The retrospective analysis of the method performances when applied to the Mw 7.8 Turkey–Syria earthquake data shows that while the earthquake location estimates converge rapidly (in 20 s after OT) to stable and near accurate values, the magnitude increases with time reaching the final, stable values at about 60 s after OT. This peculiar behavior can be explained by a time-varying moment rate function that achieves its peak at about the same time according to recent source time function determinations from kinematic rupture modeling studies. The slow magnitude rise with time is the main cause of initial underestimation of peak ground shaking either obtained from GMPE relation or from onsite P-amplitude. For this reason, setting a peak motion threshold corresponding to a level of *light perceived shaking* ($\boldsymbol{I_{MM}=IV}$) an alert issued within 10–20 s after OT shows to be successful in predicting PGV above the threshold in most of strong motion sites. On the other hand, increasing the alert threshold ($\boldsymbol{I_{MM}=VI}$, *strong perceived shaking*) more time is needed to obtain PGV predictions above the threshold and the ratio between successful and missed/false alerts is initially unfavorable (smaller or equal to 1), while becoming stable and acceptable around 8–9 at 60–70 s after OT.

For an effective implementation of a shaking-forecast, time-evolutive early warning system, like the one used in this work, the alert threshold should be set according to the specific user needs and to the impact of the emergency measure that is adopted. The adoption of a low alert threshold, in general, causes an increase of the number of false against missed alerts. In cases of large earthquakes, the present study shows that, depending on the time evolution of the earthquake source time function, the use of a low alert threshold allows for relatively large lead-times available for safety emergency actions with the benefit of high reliable strong-shaking prediction.

We also found that the predicted potential damage zone as inferred from early recorded P-waves well delineates the geometry of the rupturing fault and tracks with a high precision the space-time rupture evolution. This observation opens new perspectives in the earthquake early warning research field, showing that details of the ongoing rupture could be inferred by the radiated and faster propagating P-wave field. Information about initial rupture length and direction, could indeed be useful to better model the peak motion attenuation in presence of significant rupture directivity and with a higher accuracy that the presently assumed point-source approximation.

Method

We briefly summarize the algorithms in the following paragraphs, while the in-depth description is available in the reference literature[5]. The system is designed to process the 3-component, ground motion acceleration records, as acquired by a real-time, dense network deployed in the earthquake epicentral area.

The first P-wave arrival time signals are detected by the real-time FilterPicker 5 algorithm[24] on the vertical component of the acceleration waveforms. The real-time location estimate is then obtained by using the algorithm RTLoc[25] which is a probabilistic method that uses the triggered and the not-yet-triggered stations to perform the hypocentral estimations. Starting from the P-wave arrival time, the initial peak amplitude parameters, P_a, P_v and P_d, are measured at each station as the absolute, maximum value of the vertical component of acceleration, velocity, and displacement, respectively, in an expanded P-wave time window. The measures are repeated every 0.5 s and are stopped at the expected arrival of the S-waves, as predicted by the earthquake location.

The real-time moment magnitude (M_W) is obtained by averaging the single magnitude estimates derived from the three P-peak amplitude parameters (P_a, P_v and P_d), measured at all the station picked at the time of the measurement, with a minimum number of ten. However, the minimum number of stations to declare the event can be set by the user. Given a recording station at hypocentral distance R, for each parameter, we use a region-specific calibrated empirical attenuation relationship to estimate the moment magnitude, having the form $\log P_x = A + BM_W + C\log R$, where x = (a,v,d), R is the hypocentral distance and A,B,C are the coefficients estimated by a linear regression[26,27].

For the calibration of the empirical scaling relationships, we used the strong motion records of 6 events of the February,6,2023 Turkey–Syria main and aftershock sequence in the magnitude range 4.3–7.8 (see Supplementary Information, Table S1). The coefficients A, B and C are shown in Table S2 of the Supplementary Information. For a given station i and for each time step t, the magnitude value is obtained by the weighted average of all the available predictions.

Weights are inversely proportional to the squared standard deviation of each empirical scaling relationships. The peak ground motion in the region of interest is then predicted by combining two different approaches, one for the recording sites and another for the *virtual* nodes, i.e., the not-instrumented grid nodes, as described below. At the recording sites, measured P_a^t, P_v^t, P_d^t are jointly used to predict the expected PGV, based on a region-specific empirical scaling relationship of the form: $\log \mathrm{PGV} = \mathrm{A}\prime + \mathrm{B}\prime \log P_x$, where x = (a,v,d), the P-wave amplitude $\mathrm{P_x}$ is measured on the vertical component and the PGV is computed as the geometric mean between the two peak values recorded on the EW and NS ground motion components. For the measurement we took a variable time window from the first-P-arrival time (manually picked) to the theoretical S-arrival time, in order to prevent the contamination of the P-wave signal by S wave phases. Single and double numerical integrations are performed to obtain the velocity and displacement records and a fourth order, high-pass Butterworth filter (with a corner frequency of 0.01 Hz) is applied before each integration operation. Table S3 and Fig. S2 of the Supplementary Information show the empirical scaling relationships and the estimated coefficients. The predicted value of $\log PGV$ and its uncertainty at any time t are therefore obtained as the weighted average of the three estimated $\log PGV_x^t$ values. Furthermore, the predicted PGV from the vertical $\mathrm{P_x}$ amplitude is continuously compared to the PGV value measured on the horizontal components. At any time along the waveform, the maximum between these two values is used as the peak ground motion estimate. At the not-instrumented sites, at each time step t, the prediction of PGV is obtained using a physics-based, interpolation algorithm, like the one used for the shake-map computation[28]. It combines the available information from recording stations (on-site approach) with the available regional ground motion prediction equation (GMPE) and real-time estimates of earthquake location and magnitude (network-based approach). Details can be found in ref. 5. The final output is the predicted PGV *vs*. time at any position of the area around the earthquake source, which can be finally converted to instrumental intensity through empirical relations. In this application we used the $\mathrm{I_{MM}}$ vs PGV law proposed by Faenza and Michelini[18] (in Supplementary Information we present the results obtained using other two empirical laws).

Data availability

The waveform data used for the playback analysis in the study are available at AFAD bulletin website via https://tdvms.afad.gov.tr/list-station/543428/37.043/37.288 with free access. All the waveforms used for the calibration of the empirical laws are available at the same website. The grids to perform the location were calculated using the software NLLoc by A. Lomax, available at https://github.com/alomax/NonLinLoc, with a velocity model specific for the area[29]. Other data that are used to perform the Earthquake Early Warning simulations and waveform playback are available at https://doi.org/10.5281/zenodo.11103858.

Code availability

Analysis is performed using MATLAB Version: 9.11.0.1837725 (R2021b, academic licence) used for calibration of the empiric laws. The same software was used to produce Figs. 2, 3 and 4. Maps were prepared using the GMT[30] free software and its python version, PyGMT (details at https://www.pygmt.org/dev/index.html). The EEWS software used (QuakeUp) and is available at https://doi.org/10.5281/zenodo.11103858.

Received: 17 February 2024; Accepted: 10 June 2024;
Published online: 17 June 2024

References

1. Hoshiba, M., Kamigaichi, O., Saito, M., Tsukada, S. Y. & Hamada, N. Earthquake early warning starts nationwide in Japan. *Eos Trans. AGU* **89**, 73–74 (2008).
2. Allen, R. M. & Melgar, D. Earthquake early warning: advances, scientific challenges, and societal needs. *Annu. Rev. Earth Planet. Sci.* **47**, 361–388 (2019).
3. Clinton, J., Zollo, A., Marmureanu, A., Zulfikar, C. & Parolai, S. State-of-the-art and future of earthquake early warning in the European region. *Bull. Earthq. Eng.* **14**, 2441–2458 (2016).
4. Hoshiba, M. Real-time prediction of impending ground shaking: review of wavefield-based (Ground-Motion-Based) method for earthquake early warning. *Front. Earth Sci*. **9** https://doi.org/10.3389/feart.2021.722784 (2021).
5. Zollo, A., Colombelli, S., Caruso, A., Elia, L. An evolutionary shaking-forecast-based earthquake early warning method. *Earth Space Sci.* **10** https://doi.org/10.1029/2022EA002657 (2023).
6. Colombelli, S. & Zollo, A. Fast determination of earthquake magnitude and fault extent from real-time P-wave recordings. *Geophys. J. Int.* **202**, 1158–1163 (2015).
7. Caruso, A., Colombelli, S., Elia, L., Picozzi, M., & Zollo, A. An onsite alert level early warning system for Italy. *J. Geophys. Res. Solid Earth* **122** https://doi.org/10.1002/2016JB01340 (2017).
8. Zollo, A., Caruso, A., De Landro, G., Colombelli, S. & Elia, L. A Bayesian method for real-time earthquake location using multiparameter data. *J. Geophys. Res. Solid Earth* **126**, e2020JB020359 (2021).
9. Reilinger, R. et al. GPS constraints on continental deformation in the Africa-Arabia-Eurasia continental collision zone and implications for the dynamics of plate interactions. *J. Geophys. Res.* **111**, B05411 (2006).
10. Melgar, D. et al. Sub- and super-shear ruptures during the 2023 Mw 7.8 and Mw 7.6 earthquake doublet in SE Türkiye. *Seismica* **2** https://doi.org/10.26443/seismica.v2i3.387 (2023).
11. Liu, C. et al. Complex multi-fault rupture and triggering during the 2023 earthquake doublet in southeastern Türkiye. *Nat. Comm.* **14**, 5564 (2023).
12. US Geological Survey. Event page of the M7.8 Kahramanmaraş Earthquake Sequence. https://earthquake.usgs.gov/earthquakes/eventpage/us6000jllz/executive (2023).
13. Colombelli, S. et al. Evidence for a difference in rupture initiation between small and large earthquakes. *Nat. Commun.* **5**, 3958 (2014).
14. Colombelli, Simona, Festa, Gaetano & Zollo, Aldo Early rupture signals predict the final earthquake size. *Geophys. J. Int.* **223**, 692–706 (2020).

15. Shearer, P. M., Abercrombie, R. E., Trugman, D. T. & Wang, W. Comparing EGF methods for estimating corner frequency and stress drop from *P* wave spectra. *J. Geophys. Res. Solid Earth* **124**, 3966–3986 (2019).
16. International Seismological Centre. On-line Bulletin https://doi.org/10.31905/D808B830 (2023).
17. Xu, Chenyu et al. Rapid source inversions of the 2023 SE Türkiye earthquakes with teleseismic and strong-motion data. *Earthq. Sci.* **36**, 316–327 (2023).
18. Faenza, Licia & Michelini, Alberto Regression analysis of MCS intensity and ground motion parameters in Italy and its application in ShakeMap. *Geophys. J. Int.* **180**, 1138–1152 (2010).
19. Zhang, Y., et al. Geometric controls on cascading rupture of the 2023 Kahramanmaraş earthquake doublet. *Nat. Geosci.* https://doi.org/10.1038/s41561-023-01283-3 (2023).
20. Abdelmeguid, M. et al. Dynamics of episodic supershear in the 2023 M7.8 Kahramanmaraş/Pazarcik earthquake, revealed by near-field records and computational modeling. *Commun. Earth Environ.* **4**, 456 (2023).
21. Petersen, G. M. et al. The 2023 Southeast Türkiye seismic sequence: rupture of a complex fault network. *Seismic Rec.* **3**, 134–143 (2023).
22. Palo, M., Zollo, A., Evidence for small-scale segmented fault rupture along the East Anatolian Fault during the Mw 7.8 2023 Kahramanmaraş earthquake (preprint). In Review. https://doi.org/10.21203/rs.3.rs-3487042/v1 (2023).
23. Kodera, Y. Real-time detection of rupture development: earthquake early warning using *P* waves from growing ruptures. *Geophys. Res. Lett.* **45**, 156–165 (2018).
24. Lomax, A., Satriano, C. & Vassallo, M. Automatic picker developments and optimization: FilterPicker—A robust, broadband picker for real-time seismic monitoring and earthquake early-warning. *Seismol. Res. Lett.* **83**, 531–540 (2012).
25. Satriano, C., Lomax, A. & Zollo, A. Real-time evolutionary earthquake location for seismic early warning. *Bull. Seismol. Soc. Am.* **98**, 1482–1494 (2008).
26. Wu, Y. M., Yen, H. Y., Zhao, L., Huang, B. S. & Liang, W. T. Magnitude determination using initial P waves: a single-station approach. *Geophys. Res. Lett.* **33**, L05306 (2006).
27. Zollo, A., Lancieri, M. & Nielsen, S. Earthquake magnitude estimation from peak amplitudes of very early seismic signals on strong motion. *Geophys. Res. Lett.* **33**, L23312 (2006).
28. Worden, C. B. et al. A revised ground-motion and intensity interpolation scheme for ShakeMap. *Bull. Seismol. Soc. Am.* **100**, 3083–3096 (2010).
29. Melgar, Diego et al. Rupture kinematics of 2020 January 24 M_w 6.7 Doğanyol-Sivrice, Turkey earthquake on the East Anatolian Fault Zone imaged by space geodesy. *Geophys. J. Int.* **223**, 862–874 (2020).
30. Wessel, P., Smith, W. H. F., Scharroo, R., Luis, J. & Wobbe, F. Generic mapping tools: improved version released. *EOS Trans.* **94**, 409–410 (2013).

Acknowledgements

The research was funded by the EU through the project GOBEYOND (GA 101121135 - HORIZON-CL3-2022-DRS-01) and by the Italian Ministry of University and Research through 1/ the National Operative Program PON-AIM AIM1834927 – 3, 2/ the project PNRR RETURN, and 3/ the project PNRR: "Monitoring Earth Evolution and Tectonics – MEET", CUP D53C22001400005

Author contributions

R.R. performed the simulations in play-back mode using the earthquake platform QuakeUP, performed all the data analysis, empirical attenuation relation calibrations and prepared the figures, participated in the interpretation of the results; contributed to the article writing. S.C. contributed to the validation of the results of the retrospective performance analysis of the EEWS, designed the figures and tables; participated in the interpretation of the results; wrote the original draft. L.E. developed the version of the platform for EEW Quake UP and prepared runs and utilities for the simulation tests for the specific case of application, participated in the interpretation of the results; wrote the original draft. A.Z. conceived and led the study; contributed to the design of validation tests; co-participated to the design of the figures and tables; participated in the interpretation of the results; wrote the original draft. A.Z. is the corresponding author. All authors contributed to finalize the manuscript.

Competing interests

The authors declare no competing interests.

Additional information

Supplementary information The online version contains supplementary material available at https://doi.org/10.1038/s43247-024-01507-3.

Correspondence and requests for materials should be addressed to Aldo Zollo.

Peer review information *Communications Earth & Environment* thanks Şerif Barış and Ali Pinar for their contribution to the peer review of this work. Primary Handling Editors: Sylvain Barbot and Joe Aslin. A peer review file is available.

Reprints and permissions information is available at http://www.nature.com/reprints

Publisher's note Springer Nature remains neutral with regard to jurisdictional claims in published maps and institutional affiliations.

Open Access This article is licensed under a Creative Commons Attribution 4.0 International License, which permits use, sharing, adaptation, distribution and reproduction in any medium or format, as long as you give appropriate credit to the original author(s) and the source, provide a link to the Creative Commons licence, and indicate if changes were made. The images or other third party material in this article are included in the article's Creative Commons licence, unless indicated otherwise in a credit line to the material. If material is not included in the article's Creative Commons licence and your intended use is not permitted by statutory regulation or exceeds the permitted use, you will need to obtain permission directly from the copyright holder. To view a copy of this licence, visit http://creativecommons.org/licenses/by/4.0/.

© The Author(s) 2024